COMBINING EXTENDED CONVOLUTIONAL AUTOENCODERS AND RESERVOIR COMPUTING FOR ACCURATE REDUCED-ORDER PREDICTIONS OF ATMOSPHERIC FLOWS

ARASH HAJISHARIFI[1], MICHELE GIRFOGLIO[2], ANNALISA QUAINI[3], AND GIANLUIGI ROZZA[1,*]

ABSTRACT. Forecasting atmospheric flows with traditional discretization methods, also called full order methods (e.g., finite element methods or finite volume methods), is computationally expensive. We propose to reduce the computational cost with a Reduced Order Model (ROM) that combines Extended Convolutional Autoencoders (E-CAE) and Reservoir Computing (RC). Thanks to an extended network depth, the E-CAE encodes the high-resolution data coming from the full order method into a compact latent representation and can decode it back into high-resolution with 75% lower reconstruction error than standard CAEs. The compressed data are fed to an RC network, which predicts their evolution. The advantage of RC networks is a reduced computational cost in the training phase compared to conventional predictive models.

We assess our data-driven ROM through well-known 2D and 3D benchmarks for atmospheric flows. We show that our ROM accurately reconstructs and predicts the future system dynamics with errors below 6% in 2D and 8% in 3D, while significantly reducing the computational cost of a full order simulation. Compared to other ROMs available in the literature, such as Dynamic Mode Decomposition and Proper Orthogonal Decomposition with Interpolation, our ROM is as efficient but more accurate. Thus, it is a promising alternative to high-dimensional atmospheric simulations.

1. INTRODUCTION

Traditionally, the accurate forecast of atmospheric flow dynamics has required multiple large-scale, time-dependent simulations based on classical, high-fidelity discretization methods (e.g., finite element methods or finite volume methods). Despite a continuous increase in computational power and tremendous advancements in such discretization methods, also called Full Order Models (FOMs), these simulations remain computationally expensive. The search for accurate alternative approaches with a reduced computational has motivated a large body of literature in recent years. For example, methods borrowed from Machine Learning have been applied to global weather forecasting. See, e.g., [1, 2, 3, 4, 5, 6, 7].

We tackle this challenge starting from a reduced order modeling perspective. Reduced Order Models (ROMs) have emerged as a powerful approach to reduce the computational cost of FOM simulations. In ROMs, the reduction in the cost is achieved by approximating the high-dimensional FOM solution in a lower dimensional space, while maintaining the essential feature of the system in its compressed representation. This makes ROMs advantageous for exploring a wide range of physical parameters or conducting long-term forecasts. A ROM model is constructed in two phases. In the first phase, called offline, a comprehensive dataset of FOM solutions, corresponding to specific time instances or/and sample physical parameters, is collected. This dataset is used to generate a reduced basis containing the compact representation of the system dynamics. The offline phase is computationally expensive, but it is performed only once. In the second phase, called online, the offline-generated reduced basis is used to quickly compute the solution for a new time instance or

[1] MATHLAB, MATHEMATICS AREA, SISSA, VIA BONOMEA 265, I-34136 TRIESTE, ITALY

[2] DEPARTMENT OF ENGINEERING, UNIVERSITY OF PALERMO, VIALE DELLE SCIENZE, ED. 7, 90128 PALERMO, ITALY

[3] DEPARTMENT OF MATHEMATICS, UNIVERSITY OF HOUSTON, 3551 CULLEN BLVD, HOUSTON TX 77204, USA

* CORRESPONDING AUTHOR: GROZZA@SISSA.IT

parameter value. This is an efficient approach for multi-query contexts arising from needs such as assessing the uncertainty in the computed solution or solving an inverse problem for parameter identification or optimization. For further details, the readers is referred to, e.g., [8, 9, 10, 11, 12, 13, 14, 15, 16].

ROMs can be classified into intrusive and non-intrusive strategies [17, 18]. The intrusive ROMs are physics-based approaches where the governing equations of the high-fidelity system are projected onto the reduced space spanned by the reduced basis computed in the offline phase. For these methods, which are also referred to as projection-based methods, one needs access to the FOM solver to perform the projection onto the reduced space [19, 20, 21, 22, 15], hence the name intrusive. On the other hand, non-intrusive ROMs rely only on the FOM solution data and for this reason they are also called data-driven. In other words, they learn the reduced space and approximate the system's dynamics from the observed data [23, 24, 25].

In this paper, we propose a non-intrusive ROM. We have preferred a non-intrusive approach because intrusive ROMs for highly nonlinear problems require hyper-reduction techniques, which are both computationally expensive and problem-specific [26, 27]. For such problems, non-intrusive ROMs tend to be more computationally efficient. Additionally, non-intrusive ROMs can leverage advanced machine learning techniques, e.g., deep learning-based approaches. These approaches have been successfully used in, e.g., FourCastNet [6], GraphCast [5], and Pangu-Weather [7] to forecast complex atmospheric systems.

This work can be viewed as an extension of our previous paper [28], which compared three "off-the-shelf" non-intrusive ROMs, namely Dynamic Mode Decomposition (DMD) [29, 30, 31, 32], Hankel Dynamic Mode Decomposition (HDMD) [33, 34, 35, 36], and Proper Orthogonal Decomposition with Interpolation (PODI) [37, 38, 39, 40, 41]. In [28], we showed that, although DMD and HDMD are designed to predict the dynamics of a system, their accuracy deteriorates rather quickly as the forecast time window expands. On the other hand, the PODI solution is accurate for the entire duration of the time interval of interest thanks to the use of interpolation with radial basis functions. However, the interpolatory nature of PODI limits its usefulness for predictions. In general, the strong limitation of all three methods is that they use *linear maps* to represent the high-dimensional FOM solution in a lower-dimensional spaces. As a result, DMD, HDMD, and PODI often struggle to reproduce and predict strongly non-linear dynamics.

Deep-learning-based ROM approaches overcome this limitation by adopting *nonlinear maps* to compress the representation of nonlinear dynamics. Several studies (e.g., [42, 43, 44, 45]) have shown that these ROMs outperform existing linear ROMs in terms of accuracy. Autoencoders (AE) are a type of neural network widely used to reduce the dimensionality of high-dimensional data, typically from images, by learning nonlinear representations [46, 47]. In our case, the images are the plots of FOM solutions. The AE learns to encode the FOM solutions into lower-dimensional latent space representation by extracting the most essential features in the data. Then, a decoder can be applied to reconstruct the data back in the original high-dimensional space from the compressed representation. Convolutional Autoencoders (CAE) [48, 49, 50] replace fully connected layers in standard AE with convolutional layers, which can capture finer details and more features of spatial correlations and thus improve the quality of compressed data representation [44, 51, 52].

We propose a novel nonlinear ROM approach that integrates an enhanced version of CAE to efficiently capture the spatial correlations (i.e., higher compression ratio and lower reconstruction error than a standard CAE), with a Reservoir Computing (RC) framework to learn the evolution of the CAE latent spaces and accurately predict their future dynamics.

RC networks, derived from Recurrent Neural Network (RNN) theory [53], process sequential data. Unlike the CAE that compresses the high-resolution FOM data (dimension of the order of tens of thousands or millions) into a compact latent space (dimension of order ten) and reconstructs it back to the original resolution, the RC does not reconstruct the high-resolution data. Instead, it maps the input data, which in our case is the latent space representation given by the CAE, to a higher dimensional reservoir state space (dimension of the order of hundreds) through reservoir nodes, with the goal of better capturing the temporal dependency in the data. Unlike other RNNs, the weights

of the recurrent connections are not trained but initialized randomly and remain fixed throughout the process. The only trainable parameters in RC networks are the output layer weights. These are trained using a simple linear regression algorithm. This simple training process significantly reduced the computational cost of RC compared to other predictive networks [54, 55, 56], like Long-Short Time Memory (LSTM) [57, 45, 58, 59, 39], Gated Recurrent Unit (GRU) [60], and Transformers [61, 62, 63, 64, 65]. In fact, LSTMs and GRUs are usually slow to train because they are sequential and, consequently, cannot exploit parallel architectures. Transformers employ an attention mechanism to avoid the sequential data processing. This mechanism enables them to effectively model long-term dependencies of a dynamical system. Despite their ability to take advantage of parallel computing, transformers are computationally expensive and memory-intensive, which makes them less efficient for real time applications. Through the combination of CAE and RC, our ROM aims to improve prediction accuracy, while keeping the computational cost low.

An alternative to nonlinear ROMs, such as the one presented in this work, is to improve the representation of nonlinear dynamics by a linear ROM though data augmentation. Data augmentation can be done using, e.g., techniques borrowed from optimal transport theory [66].

The rest of the paper is organized as follows. In Sec. 2, we state the compressible Euler equations for low Mach, stratified flows, which represent our FOM. Sec. 3 describes the details of the proposed ROM approach. Sec. 4 reports the results for three well-known benchmarks: 2D and 3D rising thermal bubble and 2D density current. Finally, Sec. 5 provides conclusions and future perspectives.

2. The full order model

We are interested in the dynamic of the dry atmosphere (i.e., no humidity) and the effects of solar radiation and ground heat flux are neglected for simplicity. In a spatial domain of interest Ω over the time interval $(0, t_f]$, the Euler equations for dry air dynamics read: find air density ρ, wind velocity $\boldsymbol{u}$, and total energy e such that

$$\frac{\partial \rho}{\partial t} + \nabla \cdot (\rho \boldsymbol{u}) = 0 \qquad \text{in } \Omega \times (0, t_f], \tag{1}$$

$$\frac{\partial (\rho \boldsymbol{u})}{\partial t} + \nabla \cdot (\rho \boldsymbol{u} \otimes \boldsymbol{u}) + \nabla p + \rho g \widehat{\mathbf{k}} = \mathbf{0} \qquad \text{in } \Omega \times (0, t_f], \tag{2}$$

$$\frac{\partial (\rho e)}{\partial t} + \nabla \cdot (\rho \boldsymbol{u} e) + \nabla \cdot (p \boldsymbol{u}) = 0 \qquad \text{in } \Omega \times (0, t_f], \tag{3}$$

where p is the pressure, $\widehat{\mathbf{k}}$ is the unit vector pointing the vertical axis z, and g is the gravitational constant. We note that eq. (1), (2), and (3) describe conservation of mass, momentum and energy, respectively. The total energy density can be written as follows:

$$e = c_v T + K + gz, \quad K = |\boldsymbol{u}|^2/2 \tag{4}$$

where c_v is the specific heat capacity at constant volume and T is the absolute temperature. Let c_p is the specific heat capacity at constant pressure. By introducing the specific enthalpy, $h = c_v T + p/\rho = c_p T$, the total energy density can be rewritten as:

$$e = h - p/\rho + K + gz, \tag{5}$$

where K is the kinetic energy density defined in (4). Then, by plugging (5) into (3) and accounting for (1), we obtain:

$$\frac{\partial (\rho h)}{\partial t} + \nabla \cdot (\rho \boldsymbol{u} h) + \frac{\partial (\rho K)}{\partial t} + \nabla \cdot (\rho \boldsymbol{u} K) - \frac{\partial p}{\partial t} + \rho g \boldsymbol{u} \cdot \widehat{\mathbf{k}} = 0 \qquad \text{in } \Omega \times (0, t_f]. \tag{6}$$

To close system (1)-(3), we need an equation of state. We assume that the dry atmosphere behaves like an ideal gas, thus we have:

$$p = \rho R T, \tag{7}$$

where R is the specific gas constant of dry air.

Let us to write the pressure as the sum of a fluctuation p' with respect to a hydrostatic term:

$$p = p_g + \rho g z + p',$$
(8)

where $p_g = 10^5$ Pa is the atmospheric pressure at the ground. By plugging (8) into (2), the momentum conservation equation can be rewritten as:

$$\frac{\partial(\rho\boldsymbol{u})}{\partial t} + \nabla \cdot (\rho\boldsymbol{u} \otimes \boldsymbol{u}) + \nabla p' + gz\nabla\rho = 0 \qquad \text{in } \Omega \times (0, t_f].$$
(9)

We focus on formulation (1),(6),(7)-(9) of the Euler equations. Note that this system does not include a dissipation mechanism. Hence, numerical errors are prone to get amplified over time, leading to numerical instabilities and eventually a simulation breakdown. There are several ways to address this problem. The easiest (and crudest) is introduce an artificial dissipation term in (9) and (6) with a constant artificial viscosity μ_a:

$$\frac{\partial(\rho\boldsymbol{u})}{\partial t} + \nabla \cdot (\rho\boldsymbol{u} \otimes \boldsymbol{u}) + \nabla p' + gz\nabla\rho - \nabla \cdot (2\mu_a\boldsymbol{\epsilon}(\boldsymbol{u})) + \nabla\left(\frac{2}{3}\mu_a\nabla \cdot \boldsymbol{u}\right) = 0 \qquad \text{in } \Omega \times (0, t_f],$$
(10)

$$\frac{\partial(\rho h)}{\partial t} + \nabla \cdot (\rho\boldsymbol{u}h) + \frac{\partial(\rho K)}{\partial t} + \nabla \cdot (\rho\boldsymbol{u}K) - \frac{\partial p}{\partial t} + \rho g\boldsymbol{u} \cdot \widehat{\mathbf{k}} - \nabla \cdot \left(\frac{\mu_a}{Pr}\nabla h\right) = 0 \quad \text{in } \Omega \times (0, t_f],$$
(11)

where $\boldsymbol{\epsilon}(\boldsymbol{u}) = (\nabla\boldsymbol{u} + (\nabla\boldsymbol{u})^T)/2$ is the strain-rate tensor and Pr is the Prandtl number. In more sophisticated approaches (see, e.g., [67, 68, 69]), μ_a varies in space and time. To the effect of the method proposed in this paper, it does not matter how μ_a is defined. Hence, we will keep it constant for simplicity. So, the starting point of our full order method is model (1),(7),(8),(10),(11), plus suitable boundary conditions that will be specified for each test problem considered in Sec. 4.

A quantity of interest for atmospheric studies is the potential temperature

$$\theta = \frac{T}{\pi}, \quad \pi = \left(\frac{p}{p_g}\right)^{\frac{R}{c_p}},$$
(12)

i.e., the temperature that a parcel of dry air would have if it were expanded or compressed adiabatically to standard pressure $p_g = 10^5$ Pa. In (12), π is the so-called Exner pressure. Similar to the splitting adopted for the pressure in (8), we split the potential temperature into a hydrostatic value θ_0, that depends only on the vertical coordinate z, and fluctuation θ' over it:

$$\theta'(x, y, z, t) = \theta(x, y, z, t) - \theta_0(z).$$
(13)

To discretize problem (1),(7),(8),(10),(11) in time and space, we proceed as follows. We choose a time step $\Delta t \in \mathbb{R}^+$ to divide time interval $(0, t_f]$ to $t^n = t_0 + n\Delta t$, with $n = 0, ..., N_{tf}$ and $t_f = 0 + N_{tf}\Delta t$. The time derivatives in (1), (10), and (11) are discretized adopting the Euler scheme. The convective terms in eq. (10) and (11) are handled semi-implicitly, while the diffusive terms are treated implicitly. On the other hand, eq. (1) is solved explicitly. For the space discretization, we adopt a second-order finite volume scheme. For this, the computational domain Ω is divided into cells or control volumes Ω_i, with $i = 1, \ldots, N_c$, where N_c is the total number of cells in the mesh. To decouple the computation of the pressure from velocity, we adopt the PISO algorithm [70, 71, 72]. All of the above choices are so that we can design an efficient splitting method for the complex coupled problem at hand. The reader interested in more details about our numerical approach is referred to [68, 73].

The above full order model is implemented in GEA (Geophysical and Environmental Applications) [74, 75, 67, 68], an open-source package for atmosphere and ocean modeling based on the finite volume C++ library OpenFOAM®.

It is important to stress that, although we have made specific choices for the full order method, the reduced order model presented in the next section can be applied to data generated by any other full order method.

3. The reduced order model

Despite being efficient, the full order method described in the previous section can be computationally expensive if one is interested in simulating atmospheric flows over large computational domains and/or for long periods of time. In fact, the FOM solution is associated to a large number of degrees of freedom and, hence, it is high-dimensional. Through the ROM, we aim at approximating the FOM solution in a space with a reduced dimension while preserving the main dynamical features.

We will present our method to obtain the ROM approximation for variable θ':

$$\theta'_h(\boldsymbol{x}, t) \approx \theta'_r(\boldsymbol{x}, t), \tag{14}$$

where θ'_r is the ROM approximation of the FOM solution θ'_h. However, the same method can be applied to find any other variable of interest.

The preliminary step to find θ'_r is to collect the so-called snapshots, i.e., the FOM solutions at a given time, $\theta'_h(\boldsymbol{x}, t^i) \in \mathbb{R}^{N_c}$, with $i = 1, \ldots, N_t$. The subsequent steps involve:

- a Convolutional Autoencoder (CAE), or its enhanced version, to encode the snapshots to a compressed representation, the so-called latent space representation;
- a Reservoir Computing (RC) framework to model the temporal evolution of the latent space representation.

Then, the CAE decodes the predicted latent spaces to obtain the associated high-dimensional approximation, i.e., the actual quantity of interest.

In the subsections below, we provide more details about the CAE and the RC framework, which constitute the main building blocks of our ROM.

3.1. Convolutional Autoencoders and Extended Convolutional Autoencoders.
Convolutional autoencoders [44, 51, 45] are neural networks that learn to map the input data to a lower representation [46, 76]. They take in a two-dimensional spatial structured data instance, i.e., an image, which in our case plots a computed solution, and process it until a one-dimensional vector representation is produced. This operation is performed by a convolutional neural network and it extracts meaningful features from the input image. Since we are considering a time-dependent problem, our image evolves in time and so will its one-dimensional vector representation. It is logical to assume that another convolutional neural network could take in the one-dimensional vector representation and reconstruct the image by, in some sense, reversing the feature extraction process. A convolutional autoencoder performs both the feature extracting (encoder) and the image reconstruction (decoder) with convolutional neural networks. The convolutional layers enable the network to capture spatial patterns and extract correlations more effectively from high-dimensional data [48, 49, 51].

The encoder part of the CAE maps the input data $\theta'_h(\boldsymbol{x}, t)$ to its latent space representation $\boldsymbol{z}(t) \in \mathbb{R}^{N_d}$, with $N_d \ll N_c$, through a sequence of convolutional layers $l = 1, \ldots, L$. See Fig. 1. These layers gradually decrease spatial resolution to generate a compact representation in the final layer that captures the spatial pattern of the high-resolution input data. Formally, we can write the encoding process as:

$$\boldsymbol{z}(t) = \mathcal{E}(\theta'_h(\boldsymbol{x}, t)), \tag{15}$$

where $\mathcal{E} : \mathbb{R}^{N_c} \to \mathbb{R}^{N_d}$. In each layer l, a set of filters is convolved over the input data to extract the spatial features. The number of filters applied in each layer is denoted with N_f^l for $l = 1, \ldots, L$. The values of L and N_f^l are hyperparameters of the network that determine the feature extraction capacity overall and at each layer.

The decoder part of the CAE reconstructs the approximation $\theta'_r(\mathbf{x}, t)$ from latent spaces $\boldsymbol{z}(t)$ using the transposed convolution layers, which are called deconvolutional layers. See Fig. 1. This operation is not a direct mathematical inversion of the encoder. Instead, these layers learn a mapping to approximate the inverse process, i.e., to perform upsampling and generate the approximation of
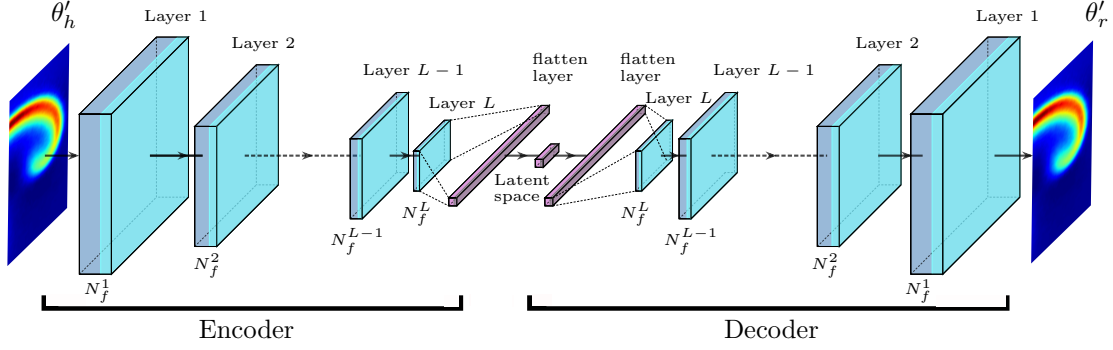
FIGURE 1. CAE architecture with encorder and decoder that feature L layers. For each layer l, with $l = 1, \ldots, L$, N_f^l is the number of applied filters.

the FOM solution. Formally, this process can be written as:

$$\theta_r'(\boldsymbol{x}, t) = \mathcal{D}(\boldsymbol{z}(t)), \tag{16}$$

where $\mathcal{D} : \mathbb{R}^{N_d} \to \mathbb{R}^{N_c}$. Through an optimization process, the CAE is trained to minimize the reconstruction error between the input data and the decoder's output, thereby ensuring that the latent representation is able to capture the most essential nonlinear spatial features of the system.

Although standard CAEs are generally effective in capturing spatial patterns in image, for images stemming from the numerical approximation of complex flows their capability is not sufficient to reconstruct the FOM solution.

To overcome this limitation, we consider a new architecture called Extended Convolutional Autoencoder (E-CAE). In this network, which is inspired by modern deep learning architectures such as VGGNet[77, 78], ResNet [79], and DenseNet [80], additional convolutional layers are stacked on top of the primary layer at each resolution level, i.e., at every layer l, with $l = 1, \ldots, L$, we apply n_f sets of N_f^l filters. See Fig. 2. This is meant to increase the network depth and enhance feature extraction capability, so that the network can learn more complex patterns before encoding them into the latent space. For the results in Sec. 4, we will use the same value of n_f for all the layers. Because more features will be extracted by the E-CAE, we add so-called dense layers between the flatten layer and the latent space to further compress the data and make the overall dimensionality reduction smoother. These dense layers are added for both the encoder and the decoder and they are expected to help with faster convergence and lower reconstruction error.

3.2. **Reservoir Computing.** RC networks [81, 55, 82] are derived from recurrent neural network theory and map input signals into higher dimensional spaces through the dynamics of a non-linear system called reservoir. The idea in RC networks is to use recursive connections within neural networks to create complex dynamical systems. RC networks can be seen as a generalization of echo state networks (ESNs - see, e.g., [83]) and have the advantage of a straightforward and low-cost training process. Fig. 3 illustrates the main components of a typical ESN: i) an input layer, which in our case takes in the latent space representation of the FOM solution at time t (i.e., $\boldsymbol{z}(t)$ in (15)); ii) a hidden (between the visible input and output) layer of randomly connected neurons, i.e., the so-called reservoir node; and iii) an output layer, which returns an object belonging to a high dimensional space. The mapping to a richer space allows the RC framework to effectively capture the temporal dependency of the input signal.

Let N_h be the number of reservoir neurons. We denote with $\boldsymbol{h}(t) \in \mathbb{R}^{N_h}$ the reservoir state at time t and with $\alpha \in [0, 1]$ the so-called leak rate. The evolution of the reservoir state is described by:

$$\boldsymbol{h}(t^n) = (1 - \alpha)\boldsymbol{h}(t^{n-1}) + \alpha \tanh(\boldsymbol{W}_{\text{in}} \, \boldsymbol{z}(t^n) + \boldsymbol{W}_{\text{res}} \, \boldsymbol{h}(t^{n-1})), \tag{17}$$
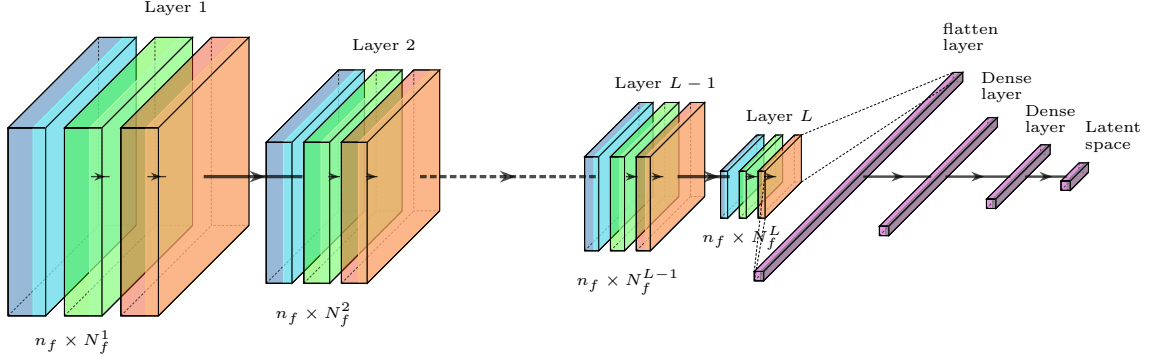
FIGURE 2. Encoder architecture of the E-CAE with L layers. For each layer l, with $l = 1, \ldots, L$, we apply n_f sets of N_f^l filters.
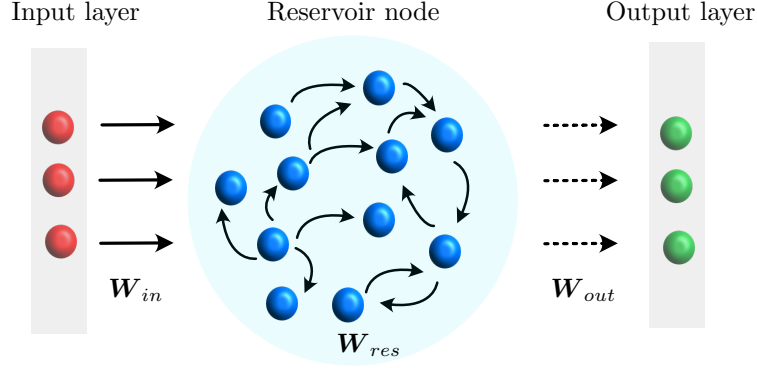

FIGURE 3. Sketch of the three main components of an RC architecture: input layer, reservoir node, and output layer. With $\boldsymbol{W}_{in}$, $\boldsymbol{W}_{res}$ and $\boldsymbol{W}_{out}$, we denote the weight matrices that define the interactions among the components.

where $\boldsymbol{W}_{\text{in}} \in \mathbb{R}^{N_h \times N_d}$ and $\boldsymbol{W}_{\text{res}} \in \mathbb{R}^{N_h \times N_h}$ are the input and reservoir weight matrices, respectively. See Fig. 3. Matrices $\boldsymbol{W}_{\text{in}}$ and $\boldsymbol{W}_{\text{res}}$ are initialized randomly and remain fixed throughout the entire process. Hyperparameter α controls the "leaking" of the previous state $\boldsymbol{h}(t^{n-1})$ into the current state $\boldsymbol{h}(t^n)$ and it determines how quickly the reservoir states are updated in response to new input $\boldsymbol{z}(t^n)$. One can say that α controls the balance between memory and reactivity in the reservoir. In fact, when α is close to one, the reservoir quickly adapts to the new input and the current reservoir state will reflect more the impact of the new input than the past information (long-term memory). On the other hand, for smaller values of α, the reservoir state is updated more slowly and it retains more information from past states. This can help the network effectively memorize past information, which is beneficial for time series with long-term memory dependency.

The matrix of the output weights $\boldsymbol{W}_{\text{out}} \in \mathbb{R}^{N_d \times (N_d + N_h)}$ is learned during the training process using linear regression. This simplification aims to reduce the expensive computational cost of training to a linear regression task. Despite it, RC remains effective in modeling and predicting complex dynamics, including chaotic time series [55]. To write down how $\boldsymbol{W}_{\text{out}}$ is obtained, let us introduce the following two matrices [55, 84]:

$$\mathbf{X} = \begin{bmatrix} \boldsymbol{z}(t^0) & \boldsymbol{z}(t^1) & \cdots & \boldsymbol{z}(t^{N_t-1}) \\ \boldsymbol{h}(t^0) & \boldsymbol{h}(t^1) & \cdots & \boldsymbol{h}(t^{N_t-1}) \end{bmatrix}, \quad \mathbf{Y} = \begin{bmatrix} \boldsymbol{z}(t^1) & \boldsymbol{z}(t^2) & \cdots & \boldsymbol{z}(t^{N_t}) \end{bmatrix}.$$

Matrix $\boldsymbol{X} \in \mathbb{R}^{(N_d+N_h) \times N_t}$ is the so-called design matrix and matrix $\boldsymbol{Y} \in \mathbb{R}^{N_d \times N_t}$ represents the target output. We recall that N_t is the number of training samples. Then, we write:

$$\boldsymbol{W}_{\text{out}} = \boldsymbol{Y} \boldsymbol{X}^T (\boldsymbol{X} \boldsymbol{X}^T + \lambda \boldsymbol{I})^{-1}, \tag{18}$$

where λ is a regularization parameter that stabilizes the solution and reduces overfitting and $\boldsymbol{I} \in \mathbb{R}^{(N_d+N_h) \times (N_d+N_h)}$ is the identity matrix.

Given input $\boldsymbol{z}(t^n)$, the reservoir state $\boldsymbol{h}(t^n)$ is computed using (17) and then the future latent space representation $\boldsymbol{z}(t^{n+1})$ is predicted using the trained output weight matrix $\boldsymbol{W}_{\text{out}}$ as follows:

$$\boldsymbol{z}(t^{n+1}) = \boldsymbol{W}_{\text{out}} \begin{bmatrix} \boldsymbol{z}(t^n) \\ \boldsymbol{h}(t^n) \end{bmatrix} \tag{19}$$

Once $\boldsymbol{z}(t^{n+1})$ is predicted with the equation above, it is fed to the decoder of the CAE or E-CAE network (16) to obtain the corresponding physical solution.

Remark 3.1. *While this work focuses on predicting one variable of interest (θ'), the proposed framework is not limited to only one physical variable and it can be extended to multi-variable predictions at the same time. The input structure of the CAE would have to be modified from a single channel to a multi-channel input, where each channel includes different physical variable at the same time instance. The CAE will learn to encode the dataset to a joint latent space that captures the dynamics of multiple variable. Once the joint latent space is obtained, the subsequent procedure remain unchanged. The RC framework is trained to predict the future dynamics of this latent space. Finally, the CAE decodes the predicted latent space to physical space where each channel represents a different predicted physical variable.*

4. NUMERICAL RESULTS

Our proposed ROM approach has been validated using two well-known atmospheric flow benchmarks where a neutrally stratified atmosphere with uniform background potential temperature is perturbed by a bubble of either warm air (2D rising thermal bubble benchmark [85, 86, 87, 69, 28]) or cold air (2D density current benchmark [85, 88, 89, 90, 69, 91, 28]). There exist several variations of these two benchmarks, with different geometry and/ or initial condition. We adopted the setting from [85] for the rising thermal bubble and the setting from [88, 91] for the density current. Through these benchmarks, we aim at checking the accuracy of our ROM technique in reconstructing the time evolution and predicting the future dynamics of the potential temperature perturbation. Results for the rising thermal bubble are presented in Sec. 4.1, while the results for the density current are discussed in Sec. 4.2. Finally, in Sec. 4.3 we consider a three-dimensional variant of the rising thermal bubble benchmark to show that the proposed ROM works as well in 3D.

4.1. **Rising thermal bubble.** We perturb a neutrally stratified atmosphere with a uniform background potential temperature of $\theta_0 = 300$ K with a circular bubble of warmer air within computational domain $\Omega = [0, 5000] \times [0, 10000]$ m^2 in the xz-plane. Over the time interval of $(0, 1020]$ s, the warm bubble rises due to buoyancy forces and transforms into a mushroom-like structure under the effect of shear stress.

The following initial temperature is prescribed:

$$\theta^0 = 300 + 2 \left[1 - \frac{r}{r_0} \right] \text{ if } r \le r_0 = 2000 \text{ m}, \quad \theta^0 = 300 \text{ otherwise}, \tag{20}$$

where $(x_c, z_c) = (5000, 2000)$ m represents the center and $r = \sqrt{(x-x_c)^2 + (z-z_c)^2}$ defines the radius of the bubble [85, 86]. The initial density and initial specific enthalpy are given by:

$$\rho^0 = \frac{p_g}{R\theta_0} \left(\frac{p}{p_g} \right)^{c_v/c_p} \quad \text{with} \quad p = p_g \left(1 - \frac{gz}{c_p \theta^0} \right)^{c_p/R}, \tag{21}$$

$$h^0 = c_p \theta^0 \left(\frac{p}{p_g} \right)^{\frac{R}{c_p}}, \tag{22}$$

with $p_g = 10^5$ Pa, $c_p = R + c_v$, $c_v = 715.5$ J/(Kg K), and $R = 287$ J/(Kg K). The initial velocity field is zero everywhere. Impenetrable, free-slip boundary conditions are imposed on all the boundaries.

We consider a uniform structured mesh with a grid size of $h = \Delta x = \Delta z = 62.5$ m. The time step is $\Delta t = 0.1$ s. We set $\mu_a = 15$ and $Pr = 1$ in (10)-(11) following [85, 68].

The original database is constructed by collecting the computed potential temperature perturbation θ' every second. This database is then divided into a training dataset and a validation dataset. As usual, the training dataset is used to train the CAE and RC networks, while the validation dataset is used to validate the ability of the CAE to reconstruct the physical space from the corresponding latent space and to asses the prediction accuracy of the RC network.

The CAE network we use for this benchmark has $L = 4$ convolutional layers with $N_f^1 = 256$, $N_f^2 = 128$, $N_f^3 = 64$, and $N_f^4 = 32$ and it gives a latent space representation with $N_d = 4$. See Fig. 1. For the RC network, we choose $N_h = 400$ reservoir neurons and set the leak rate to $\alpha = 0.0095$ and the regularization parameter to $\lambda = 0.004$

Let us analyze the model sensitivity to variations of the training-to-validation (T-to-V) dataset ratio. Tab. 1 reports the three cases we considered with different T-to-V dataset ratios. In all cases, the snapshots corresponding to the first N_t times are used to form the training set, with $N_t = 408$ for the $40\% - 60\%$ ratio, $N_t = 612$ for the $60\% - 40\%$ ratio and $N_t = 816$ for the $80\% - 20\%$ ratio. The remaining snapshots are reserved for validation. Fig. 4 shows the evolution of the CAE latent spaces for all cases reported in Tab. 1. The blue curve shows the latent space obtained from the CAE, denoted as ground truth, while the orange curve represent the latent spaces predicted by the RC network. We observe that the RC network does a poor job when only 40% of the ground truth is used for training, due to insufficient data and a relatively long prediction window. The performance improves when we use 60% of the database to predict the remaining 40%, but the improvement becomes significant only when 80% of the database is used for training. In this last case, we obtain an excellent agreement between ground truth and reconstruction/prediction for all four latent spaces.

	T-to-V dataset ratio	T Snapshots #	V Snapshots #
Case 1	40% - 60%	408	612
Case 2	60% - 40%	612	408
Case 3	80% - 20%	816	204

TABLE 1. Rising thermal bubble: training-to-validation (T-to-V) dataset ratio, number of training snapshots and validation snapshots for the three cases used for the sensitivity analysis.

We note that CAE networks introduce multiple sources of randomness, which are hard to control. This makes it difficult to obtain an identical latent space representations across different training instances. Consequently, different latent space representations may be obtained each time the CAE is trained. It is important for this representation to be as smooth (see the example in Fig. 4) as possible for our ROM to work seamlessly, as irregularities could worsen the accuracy of our predictive model.

For a quantitative assessment of the reconstructions and predictions, we compute the L^2 error between FOM and ROM solutions:

$$(23) \qquad E_{\theta'}(t) = 100 \cdot \frac{||\theta_h'(t) - \theta_r'(t)||_{L^2(\Omega)}}{||\theta_h'(t)||_{L^2(\Omega)}}.$$

Fig. 5 shows error (23) for the three T-to-V dataset ratios under consideration. In all cases, the reconstruction error (i.e., the error within the training time interval) remains low, demonstrating that the CAE is capable of accurately reconstructing the FOM solution from the latent spaces. Additionally, this suggests that the CAE can perform its reconstruction task effectively even when trained on only 40% of the database. However, the prediction error varies considerably in the three cases. For the case 1 (blue curve), the error increases rapidly after the beginning of prediction phase.
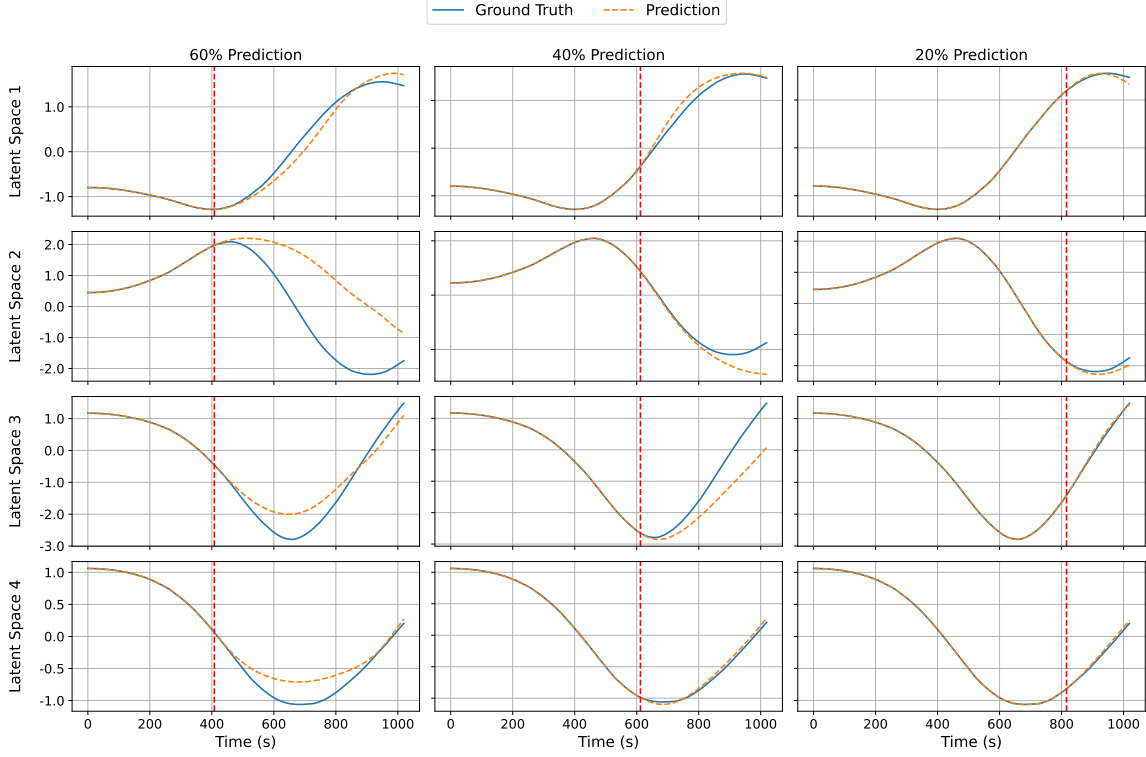
FIGURE 4. Rising thermal bubble: Time evolution of latent spaces for the different training-to-validation (T-to-V) dataset ratios listed in Tab. 1. The blue and orange dashed curves show the ground truth and the reconstructed/predicted latent spaces, respectively. The red dashed line indicates the time instance where prediction starts.

This behaviour points to a clear insufficiense of training data. For case 2 (orange curve), the error remains lower than 10% for the first 200 s of prediction, i.e., until $t = 800$ s. However, after $t = 800$ s the prediction worsens quickly. In case 3 (green curve), we obtain a low error ($< 6\%$) throughout the entire prediction phase, which lasts about 200 s. However, even in this third case, we see a sharp increase in the error towards the end of the prediction phase, indicating that one could probably not expect the error to remain low for much longer. Fig. 5 suggests that the RC network can accurately predict the future dynamic when trained on a sufficiently large amount of training data. Hence, from now on we stick to the 80%-20% T-to-V dataset ratio to analyze the performance of our ROM for this benchmark.

Fig. 6 displays a qualitative comparison between ROM and FOM solutions at five times. Out of these five time instances, the first two (i.e., $t = 255$ s and $t = 505$ s) are part of the training dataset and are meant to demonstrate the ability of the CAE to reconstruct the solution from the latent spaces. For these 2 times, we see excellent agreement between ROM and FOM solutions, as expected from Fig. 5. The remaining three time instances (i.e., $t = 930, 980, 1020$ s) belong to the validation dataset and are used to assess the accuracy of the ROM to predict the future state of the system. We observe that the ROM is able to predict the FOM results rather accurately, although at the final time $t = 1020$ s the agreement is less satisfactory. This was expected since, as shown in the sub-panel of Fig. 5, the L^2 error between FOM and ROM solutions for case 3 (80%-20% T-to-V ratio) reaches 6% at the end of simulation. The third column in Fig. 6 shows the difference between ROM and FOM solutions in absolute value with a color bar narrowed to interval $[0, 0.1]$, which corresponds to 10% of the maximum value, to better visualize the differences.
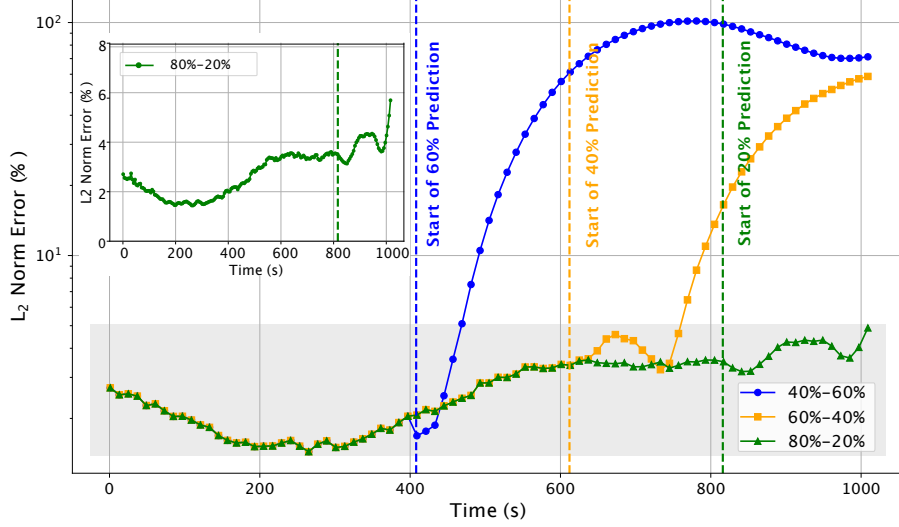
FIGURE 5. Rising thermal bubble: Time evolution of error (23) for different training-to-validation (T-to-V) dataset ratios listed in Tab. 1: $60\% - 40\%$ (blue curve), $40\% - 60\%$ (yellow curve) and $80\% - 20\%$ (green curve). The dashed vertical lines indicate the start of prediction phase for each case. The inset provides a zoomed-in view of green curve in normal scale.

All the simulations were run on a 11th Gen Intel(R) Core(TM) i7-11700 @ 2.50GHz system with 32 GB RAM. On this machine, a FOM simulation takes 65 s. The training for the CAE and RC framework, which was conducted on Google Colab with A100 GPUs, takes approximately 1500 s. The time required by the ROM to predict the latent space and reconstruct the physical solution after training phase is around less than 1 s.

4.2. **Density Current.** We perturb a neutrally stratified atmosphere with a uniform background potential temperature of $\theta_0 = 300$ K with a circular bubble of cold air within computational domain $\Omega = [0, 25600] \times [0, 6400]$ m^2 in the xz-plane. During the time interval of interest $(0, 900]$ s, the cold air experiences two primary motions: initially, the negative buoyancy generates vertical motion driving the cold air toward the ground. Upon reaching the ground, the air forms a cold front that propagates through a dominant horizontal motion, during which a complex structure with multiple vortices is created.

The initial temperature field is given by:

$$(24) \qquad \theta_0 = 300 - \theta_s[1 + \cos(\pi r)], \quad \text{if } r \leq 1, \quad \text{otherwise } \theta_0 = 300,$$

where θ_s represents the semi-amplitude of the initial temperature perturbation and it is set to 7.5 [85, 88, 89, 90, 69, 91]. The parameter r represents a normalized radial distance, calculated as:

$$(25) \qquad r = \sqrt{\left(\frac{x - x_c}{x_r}\right)^2 + \left(\frac{z - z_c}{z_r}\right)^2}.$$

with $(x_r, z_r) = (4000, 2000)$ m and $(x_c, z_c) = (0, 3000)$ m. The initial density and specific enthalpy are given by (21) and (22), respectively, while the velocity field is initialized to zero across the domain. Impenetrable, free-slip boundary conditions are imposed on all walls.

We consider a structured grid with a uniform spacing $h = \Delta x = \Delta z = 100$ m and time step is $\Delta t = 0.1$ s. We set $\mu_a = 75$ and $Pr = 1$ in (10)-(11) to stabilize the numerical solution [85, 91]. To evaluate the accuracy of our ROM model, we sample the θ' field at the frequency of 1 second, resulting in a dataset of 900 snapshots. Based on the sensitivity analysis of the training-to-validation
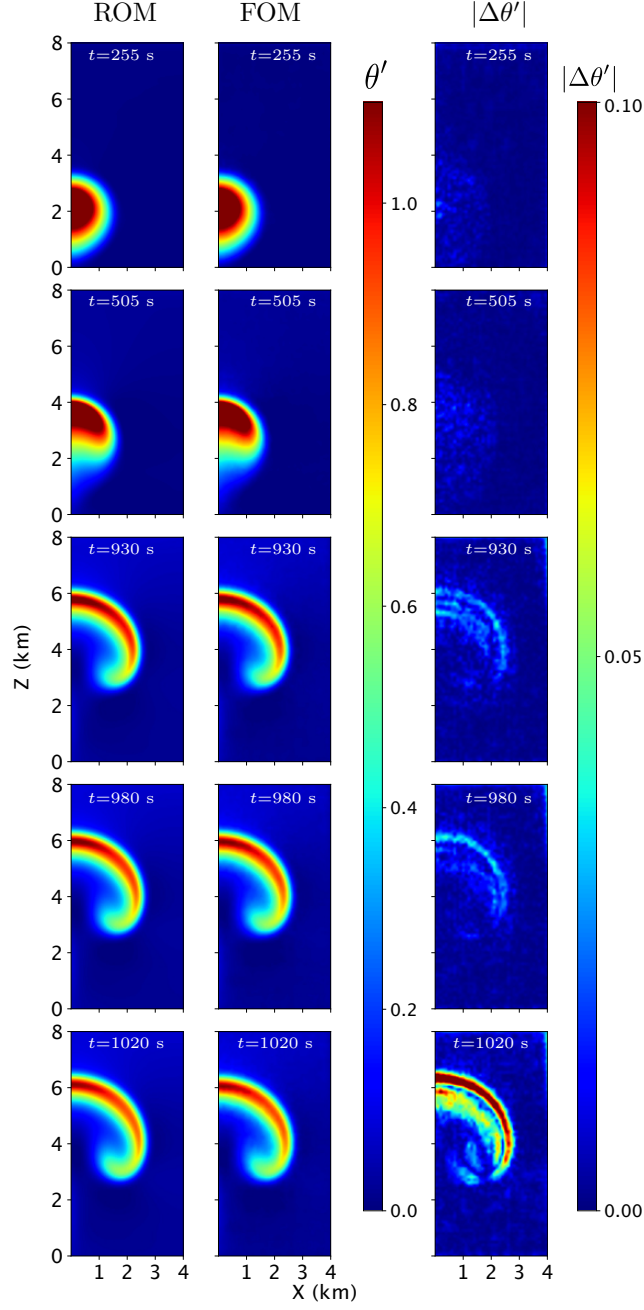
FIGURE 6. Rising thermal bubble: Comparison of the evolution of θ' given by the ROM (first column) and the FOM (second column) and their differences in absolute value (third column).

dataset ratio conducted for the previous benchmark, we use a ratio of 80%-20% (720 - 180 snapshots) to generate the training and validation datasets.

The snapshots are encoded into $N_d = 4$ latent spaces through a CAE/E-CAE and a RC network is subsequently trained on the obtained latent spaces to predict future. The CAE and E-CAE networks

for this benchmark consist of $L = 4$ convolutional layers with $N_f^1 = 512$, $N_f^2 = 256$, $N_f^3 = 128$, and $N_f^4 = 64$. The number of filters per layer is increased with respect to the benchmark in the previous section because the density current benchmark features a more complex dynamics. For the E-CAE network, we set $n_f = 3$. See Fig. 2. For the RC network, we choose $N_h = 1000$ reservoir neurons and set the leak rate to $\alpha = 0.0022$ and the regularization parameter to $\lambda = 0.0022$.

Fig. 7 shows the evolution of error (23) in the reconstruction phase $(0, 720]$ s for two convolutional autoencoder networks: CAE (orange curve) and E-CAE (blue curve). While the CAE network depicted in Fig. 1 worked well for the simpler dynamic of the warm bubble benchmark, it struggles to capture the more complex dynamic of this benchmark. The error of the CAE increases over time and reaches around 12% by time $t = 720$ s. This limitation is due to the insufficient depth of the network which constrains its ability to effectively learn the highly non-linear dynamics arising in this benchmark. From Fig. 7, it is evident that the department-wise strategy of E-CAE illustrated in Fig. 2 significantly outperforms a standard CAE: error (23) remains below 2% for most of the time interval $(0, 720]$ s, achieving 75% lower reconstruction error and fewer oscillations than the CAE. This suggests that the additional layers can successfully capture the complex dynamics, enabling the network to accurately reconstruct the physical field from its latent spaces. Hence, from the rest of the section we will present results obtained with the E-CAE.
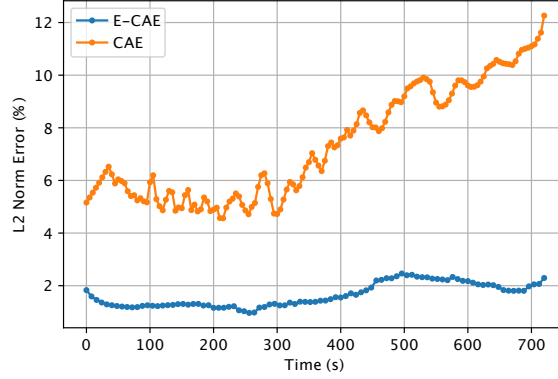

FIGURE 7. Density current: Time evolution of the L^2 error (23) between FOM and ROM solutions for CAE (orange curve) and E-CAE (blue curve).

Fig. 8 illustrates the latent spaces obtained through E-CAE (ground truth) and the latent spaces reconstructed/predicted using RC network (prediction). The excellent agreement we observe in all four panels in Fig. 8 shows the capability of the RC network to effectively learn the dynamics of compressed data representation and accurately predict their future evolution.

Fig. 9 shows the reconstruction error of the E-CAE till $t = 700$ s and the combined error (the sum of the reconstruction and prediction errors) from $t = 700$ s to $t = 900$ s. The reconstruction error remains stable at around 2% throughout the training phase while the combined error gradually increases to 4%, which is still a rather remarkable performance of the RC network in predicting the future state of latent spaces. However, once again we observe a sharp rise in the error towards the end of the prediction phase, which indicates the accuracy in the prediction might not decline quickly past $t = 900$ s.

Fig. 10 displays a qualitative comparison between ROM and FOM solutions, with their difference in absolute value, for 5 time instances. Like in the case of Fig. 6, the first two time instances (i.e., $t = 400, 600$ s) belong to the training phase and demonstrate the accuracy of the E-CAE. The close agreement that we see in the first two rows of Fig. 10 reflects the small L^2 error seen in Fig. 9 during the training phase. The last three rows in Fig. 10, corresponding to $t = 820, 850, 900$ s, show the accuracy of E-CAE and RC networks in predicting the future state of the system. The small mismatch in predicting the propagation of the cold front and the multi-rotor flow structure
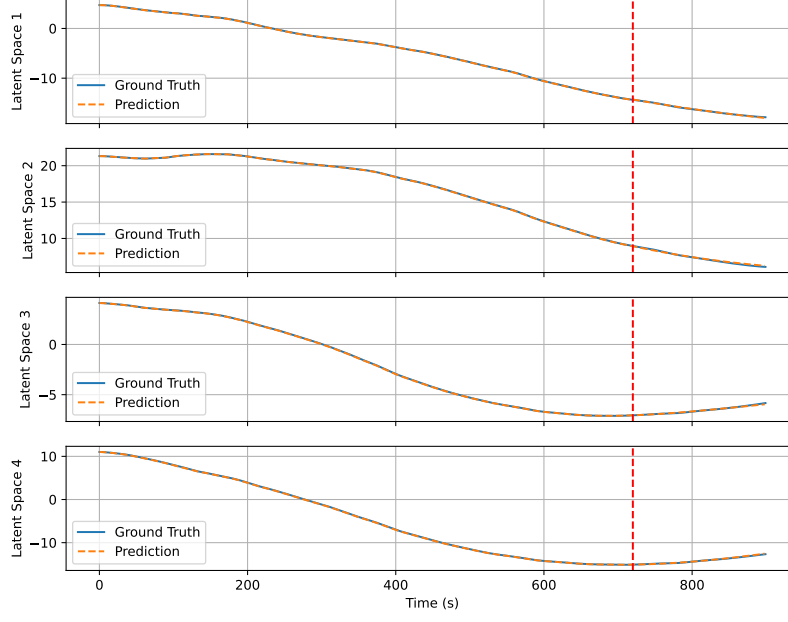
FIGURE 8. Density current: Time evolution of latent spaces obtained using E-CAE (blue curve) and reconstructed/predicted by RC framework (orange curve). The red dashed line shows the beginning of prediction phase.
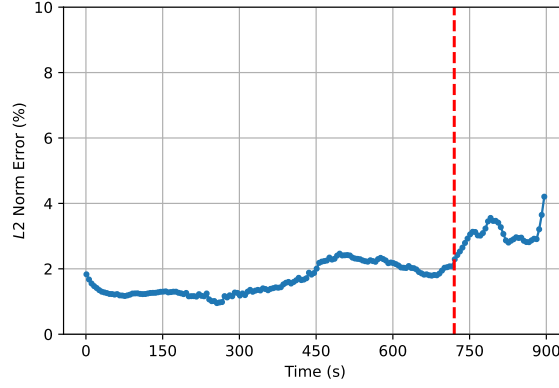

FIGURE 9. Density current: Time evolution of the L^2 error (23) between FOM and ROM solutions. The red dashed line marks the beginning of prediction.

demonstrate the accuracy of our approach. To improve the visualization of the difference between the ROM and FOM solutions in absolute value, we restricted the color bar for the third column of Fig. 10 to $[0, 0.5]$, corresponding to 4% of the maximum value.

The FOM simulation on the same local hardware mentioned at the end of Sec. 4.1 takes 286 s. The training of the CAE and RC framework takes approximately 4100 s. Then, the time needed for the ROM prediction is around 2 s.

4.3. **3D Rising Thermal Bubble.** To demonstrate that the applicability of the ROM under consideration is not limited to 2D problems, we consider a tree-dimensional variant [90, 28] of the rising thermal bubble benchmark in Sec. 4.1.
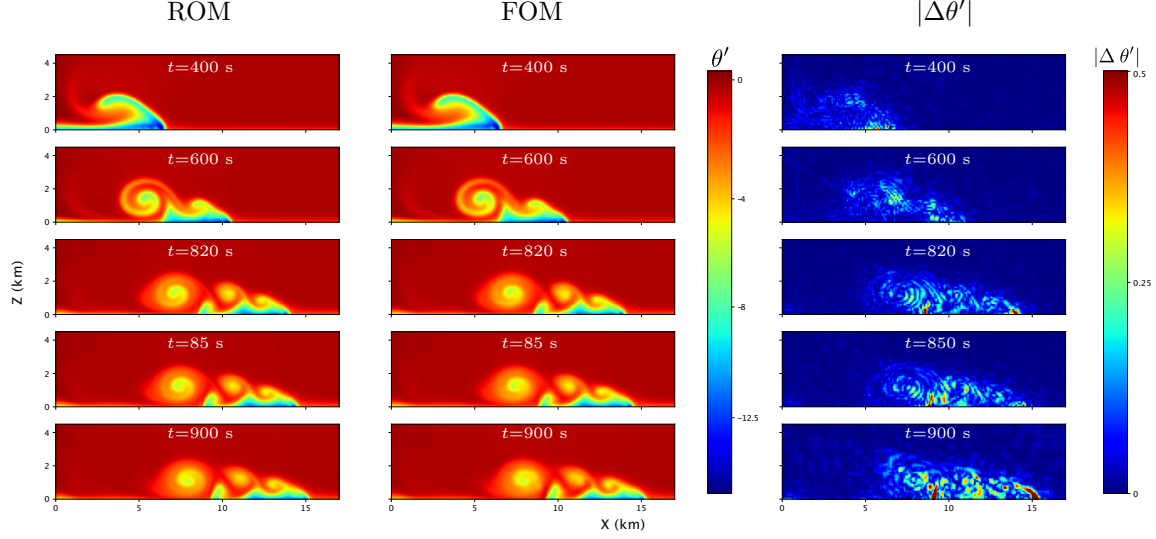
FIGURE 10. Density current: comparison of the evolution of θ' given by the ROM (first column) and the FOM (second column) and their differences in absolute value (third column).

The computational domain is a parallelepiped with dimensions $\Omega = [0, 1600] \times [0, 1600] \times [0, 4000] \, \mathrm{m}^3$. Similar to the 2D version of the benchmark, the system starts from a neutrally stratified atmosphere with uniform background potential temperature at 300 K, with a disturbance in the form of a spherical bubble of warmer air. This initial temperature field is given by:

$$(26) \qquad \theta^0 = 300 + 2 \left[1 - \frac{r}{r_0} \right] \text{ if } r \leq r_0 = 500 \, \mathrm{m}, \quad \theta^0 = 300 \text{ otherwise,}$$

with $r = \sqrt{(x - x_c)^2 + (y - y_c)^2 + (z - z_c)^2}$ and $(x_c, y_c, z_c) = (1600, 1600, 500) \, \mathrm{m}$. The initial density and enthalpy are given by (21) and (22), respectively. The initial velocity field is set to zero everywhere. Impenetrable, free-slip boundary conditions are imposed on all boundaries. The time interval of interest is $(0, 500] \, \mathrm{s}$.

We consider a structured uniform mesh of size $h = \Delta x = \Delta y = \Delta z = 40 \, \mathrm{m}$ and set the time step to $\Delta t = 0.1$ s. Following [90], we set $\mu_a = 12.5$ and $Pr = 1$.

To generate the ROM model, we sample the θ' field every second by collecting a total of 500 snapshots. This dataset is split with a T-to-V ratio of $80\% - 20\%$, i.e., we use the first 400 snapshots for training and the remaining 100 for validation. Given the excellent performance of the E-CAE network for the density current benchmark, we use the same type of network to encode the 3D field into $N_d = 4$ latent spaces, i.e., E-CAE network consists of $L = 4$ convolutional layers with $N_f^1 = 512$, $N_f^2 = 256$, $N_f^3 = 128$, and $N_f^4 = 64$ with $n_f = 3$ sets of filters at each resolution. The only difference is that for this benchmark we use the 3D CNN layer in the E-CAE network. We choose the following hyperparametrs for the RC network: $N_h = 1200$, $\alpha = 0.015$ and $\lambda = 0.00055$.

We provide a qualitative comparison of θ' computed by the ROM and the FOM in Fig. 11, which shows the results for $t = 340, 420, 500$ s. Of these three times, the first belongs to the training dataset, while the other two belong to the validation set. Just like for the 2D tests, we see that the E-CAE can accurately reconstruct the physical field from its compressed representation and the combination of E-CAE and RC networks can accurately predict the spatio-temporal state of the system with remarkable precision. In fact, we observe that the ROM accurately predicts the system dynamics up to the final time (i.e., $t = 500$ s), with only minor differences with respect to the FOM, that are mostly concentrated around the bubble.
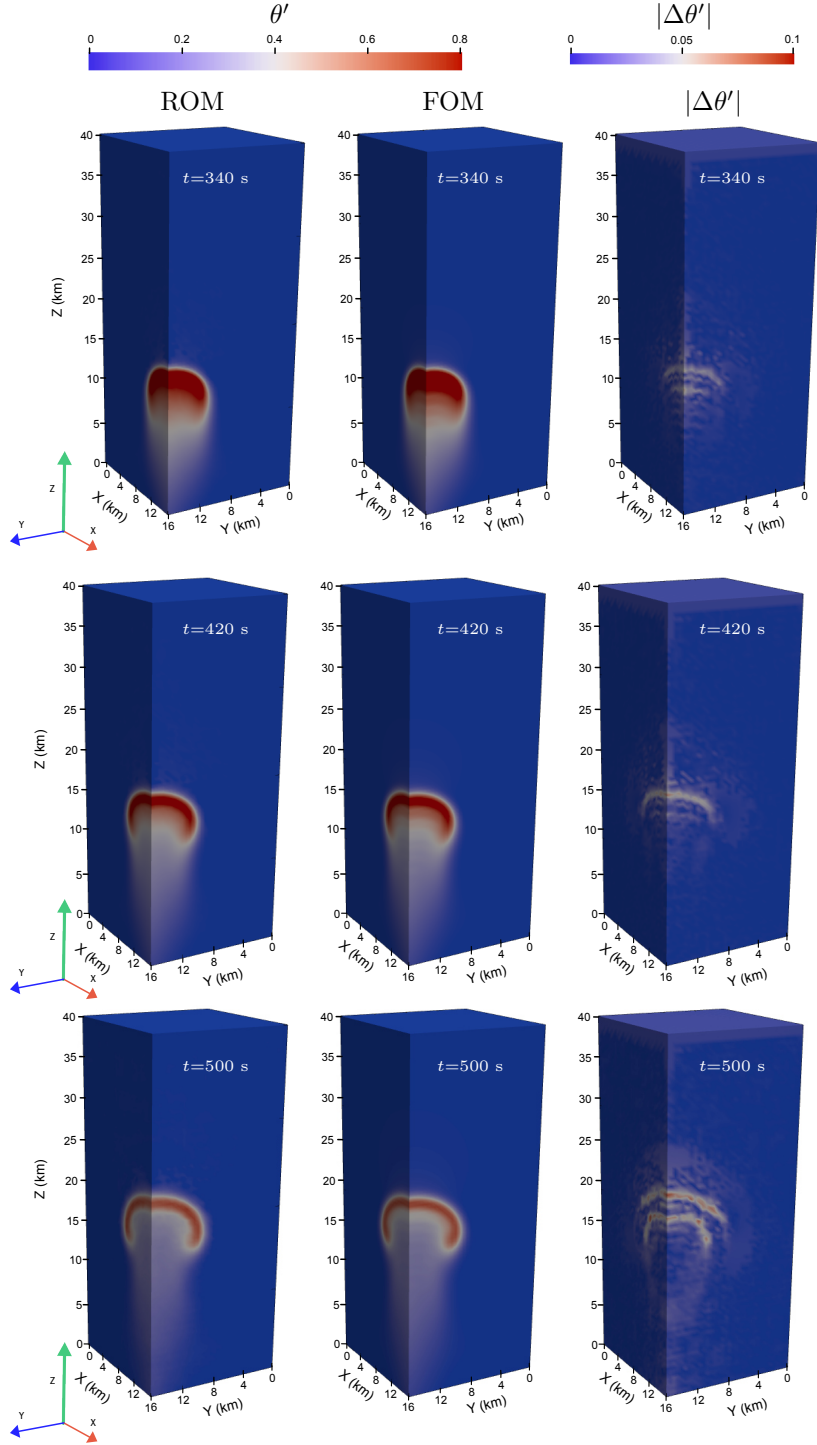
FIGURE 11. 3D rising thermal bubble: evolution of θ' given by the ROM (left column) and the FOM (right column), and their differences in absolute value (third column).
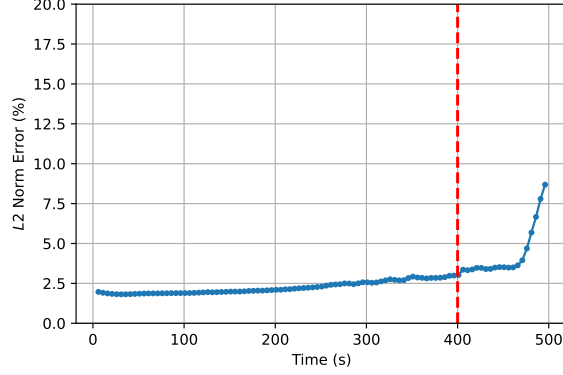
FIGURE 12. 3D rising thermal bubble: evolution of the error (23). The red dashed line indicates the beginning of the prediction phase.

To support the qualitative analysis in Fig. 11, Fig. 12 shows the evolution of error (23) for the reconstruction and prediction phases. The error in the reconstruction phase remains around 2.5%, while the prediction error gradually increases to around 8%.

We conclude with a comment on the computational times using the machine described at the end of Sec. 4.1. The FOM simulation for this test requires 4050 s. The training time of our proposed framework takes approximately 5400 s, while the ROM inference time is about 2 s.

5. CONCLUDING REMARKS

Traditional data-driven reduced order models (ROMs), such as Dynamic Mode Decomposition and Proper Orthogonal Decomposition with Interpolation, struggle to capture and accurately predict future dynamics of highly nonlinear systems. We introduced a nonlinear data-driven framework that integrates Convolutional Autoencoder (CAE) and Reservoir Computing (RC) to improve the accuracy of reduced order modeling for mesoscale atmospheric flows. Our approach compresses the high-resolution data into a low-dimensional latent space representation through a more capable version of CAE, called Extended Convolutional Autoencoders (E-CAE). Then, a RC network is used to accurately and efficiently predict the future evolution of the latent space.

We assessed our approach with three well-known benchmarks for atmospheric flows, two of which are in two dimensions, while the third is in three dimensions. We show that the E-CAE significantly improves the accuracy of spatial feature extraction when compared to standard CAEs. Moreover, we show that the RC network accurately predicts the future state of the system while significantly reducing the computational cost compared to a full order simulation. This is thanks to the fact that, unlike other RNN networks, RC only trains the output weights using a simple linear regression. The scalability of our ROM is demonstrated with the 3D benchmark.

While we believe this study represents a significant step toward a more accurate and efficient approach to accelerate atmospheric flow prediction, improvements are certainly possible. One possible improvement may come from the integration of physics-informed approaches, which are expected to enable accurate predictions over longer time intervals. If one is interested in parametric studies, neural operator-based approaches, such as DeepONet [92, 93] and Fourier Neural Operator [94] could be considered to further contain the computational cost.

6. ACKNOWLEDGMENTS

References

[1] Jaideep Pathak, Brian Hunt, Michelle Girvan, Zhixin Lu, and Edward Ott. Model-free prediction of large spatiotemporally chaotic systems from data: A reservoir computing approach. *Physical review letters*, 120(2):024102, 2018.

[2] Stephan Rasp and Nils Thuerey. Data-driven medium-range weather prediction with a resnet pretrained on climate simulations: A new model for weatherbench. *Journal of Advances in Modeling Earth Systems*, 13(2):e2020MS002405, 2021.

[3] Martin G Schultz, Clara Betancourt, Bing Gong, Felix Kleinert, Michael Langguth, Lukas Hubert Leufen, Amirpasha Mozaffari, and Scarlet Stadtler. Can deep learning beat numerical weather prediction? *Philosophical Transactions of the Royal Society A*, 379(2194):20200097, 2021.

[4] Jonathan A Weyn, Dale R Durran, and Rich Caruana. Can machines learn to predict weather? using deep learning to predict gridded 500-hpa geopotential height from historical weather data. *Journal of Advances in Modeling Earth Systems*, 11(8):2680–2693, 2019.

[5] Remi Lam, Alvaro Sanchez-Gonzalez, Matthew Willson, Peter Wirnsberger, Meire Fortunato, Ferran Alet, Suman Ravuri, Timo Ewalds, Zach Eaton-Rosen, Weihua Hu, et al. Learning skillful medium-range global weather forecasting. *Science*, 382(6677):1416–1421, 2023.

[6] Jaideep Pathak, Shashank Subramanian, Peter Harrington, Sanjeev Raja, Ashesh Chattopadhyay, Morteza Mardani, Thorsten Kurth, David Hall, Zongyi Li, Kamyar Azizzadenesheli, et al. Fourcastnet: A global data-driven high-resolution weather model using adaptive fourier neural operators. *arXiv preprint arXiv:2202.11214*, 2022.

[7] Kaifeng Bi, Lingxi Xie, Hengheng Zhang, Xin Chen, Xiaotao Gu, and Qi Tian. Accurate medium-range global weather forecasting with 3D neural network. *Nature*, 619:533–538, 2023.

[8] Benner Peter, Stefano Grivet-Talocia, Quarteroni Alfio, Rozza Gianluigi, Schilders Wil, Luis Miguel Silveira, et al. Model order reduction. volume 1: System-and data-driven methods and algorithms. 2021.

[9] Peter Benner, Wil Schilders, Stefano Grivet-Talocia, Alfio Quarteroni, Gianluigi Rozza, and Luís Miguel Silveira. *Model Order Reduction: Volume 2: Snapshot-Based Methods and Algorithms*. De Gruyter, 2020.

[10] Peter Benner, Wil Schilders, Stefano Grivet-Talocia, Alfio Quarteroni, Gianluigi Rozza, and Luís Miguel Silveira. *Model order reduction: volume 3 applications*. De Gruyter, 2020.

[11] Jan S Hesthaven, Gianluigi Rozza, and Benjamin Stamm. *Certified reduced basis methods for parametrized partial differential equations*, volume 590. Springer, 2016.

[12] Muhammad Haris Malik. *Reduced Order Modeling for Smart Grids' Simulation and Optimization*. PhD thesis, École centrale de Nantes; Universitat politécnica de Catalunya, 2017.

[13] Gianluigi Rozza, Dinh Bao Phuong Huynh, and Anthony T Patera. Reduced basis approximation and a posteriori error estimation for affinely parametrized elliptic coercive partial differential equations: application to transport and continuum mechanics. *Archives of Computational Methods in Engineering*, 15(3):229–275, 2008.

[14] Peter Benner, Mario Ohlberger, Albert Cohen, and Karen Willcox. *Model reduction and approximation: theory and algorithms*. SIAM, 2017.

[15] Peter Benner, Serkan Gugercin, and Karen Willcox. A survey of projection-based model reduction methods for parametric dynamical systems. *SIAM review*, 57(4):483–531, 2015.

[16] Pierfrancesco Siena, Paquale Claudio Africa, Michele Girfoglio, and Gianluigi Rozza. On the accuracy and efficiency of reduced order models: Towards real-world applications. *Advances in Applied Mechanics*, 59:245–288, 2024.

[17] Gianluigi Rozza, Giovanni Stabile, and Francesco Ballarin. *Advanced reduced order methods and applications in computational fluid dynamics*. SIAM, 2022.

[18] D Xiao, CE Heaney, F Fang, L Mottet, R Hu, DA Bistrian, E Aristodemou, IM Navon, and CC Pain. A domain decomposition non-intrusive reduced order model for turbulent flows. *Computers & Fluids*, 182:15–27, 2019.

[19] Kevin Carlberg, Matthew Barone, and Harbir Antil. Galerkin v. least-squares petrov–galerkin projection in nonlinear model reduction. *Journal of Computational Physics*, 330:693–734, 2017.

[20] Ricardo Reyes and Ramon Codina. Projection-based reduced order models for flow problems: A variational multiscale approach. *Computer Methods in Applied Mechanics and Engineering*, 363:112844, 2020.

[21] Clarence W Rowley, Tim Colonius, and Richard M Murray. Model reduction for compressible flows using pod and galerkin projection. *Physica D: Nonlinear Phenomena*, 189(1-2):115–129, 2004.

[22] Renee Swischuk, Laura Mainini, Benjamin Peherstorfer, and Karen Willcox. Projection-based model reduction: Formulations for physics-based machine learning. *Computers & Fluids*, 179:704–717, 2019.

[23] Michael Schlegel and Bernd R Noack. On long-term boundedness of galerkin models. *Journal of Fluid Mechanics*, 765:325–352, 2015.

[24] Dunhui Xiao, Fangxin Fang, Andrew G Buchan, Christopher C Pain, Ionel Michael Navon, Juan Du, and G Hu. Non-linear model reduction for the navier–stokes equations using residual deim method. *Journal of Computational Physics*, 263:1–18, 2014.

[25] Jan Östh, Bernd R Noack, Siniѵsa Krajnović, Diogo Barros, and Jacques Borée. On the need for a nonlinear subscale turbulence term in pod models as exemplified for a high-reynolds-number flow over an ahmed body. *Journal of Fluid Mechanics*, 747:518–544, 2014.

[26] Maxime Barrault, Yvon Maday, Ngoc Cuong Nguyen, and Anthony T Patera. An 'empirical interpolation'method: application to efficient reduced-basis discretization of partial differential equations. *Comptes Rendus Mathematique*, 339(9):667–672, 2004.

[27] Saifon Chaturantabut and Danny C Sorensen. Nonlinear model reduction via discrete empirical interpolation. *SIAM Journal on Scientific Computing*, 32(5):2737–2764, 2010.

[28] Arash Hajisharifi, Michele Girfoglio, Annalisa Quaini, and Gianluigi Rozza. A comparison of data-driven reduced order models for the simulation of mesoscale atmospheric flow. *Finite Elements in Analysis and Design*, 228:104050, 2024.

[29] J Nathan Kutz, Steven L Brunton, Bingni W Brunton, and Joshua L Proctor. *Dynamic Mode Decomposition: data-driven modeling of complex systems*. SIAM, 2016.

[30] Peter J Schmid. Dynamic mode decomposition of numerical and experimental data. *Journal of fluid mechanics*, 656:5–28, 2010.

[31] Peter J Schmid, Larry Li, Matthew P Juniper, and O Pust. Applications of the dynamic mode decomposition. *Theoretical and computational fluid dynamics*, 25:249–259, 2011.

[32] Jonathan H Tu, Clarence W Rowley, Dirk M Luchtenburg, Steven L Brunton, and J Nathan. Kutz. On dynamic mode decomposition: Theory and applications. *Journal of Computational Dynamics*, 1:391–421, 2014/12.

[33] Hassan Arbabi and Igor Mezic. Ergodic theory, dynamic mode decomposition, and computation of spectral properties of the Koopman operator. *SIAM Journal on Applied Dynamical Systems*, 16(4):2096–2126, 2017.

[34] Christopher W Curtis, D Jay Alford-Lago, Erik Bollt, and Andrew Tuma. Machine learning enhanced hankel dynamic-mode decomposition. *Chaos: An Interdisciplinary Journal of Nonlinear Science*, 33(8), 2023.

[35] Keisuke Fujii, Naoya Takeishi, Benio Kibushi, Motoki Kouzaki, and Yoshinobu Kawahara. Data-driven spectral analysis for coordinative structures in periodic human locomotion. *Scientific reports*, 9(1):16755, 2019.

[36] Huiming Jiang, Jin Chen, Guangming Dong, Tao Liu, and Gang Chen. Study on Hankel matrix-based SVD and its application in rolling element bearing fault diagnosis. *Mechanical systems and signal processing*, 52:338–359, 2015.

[37] Nirav Vasant Shah, Michele Girfoglio, Peregrina Quintela, Gianluigi Rozza, Alejandro Lengomin, Francesco Ballarin, and Patricia Barral. Finite element based Model Order Reduction for parametrized one-way coupled steady state linear thermo-mechanical problems. *Finite Elements in Analysis and Design*, 212:103837, 2022.

[38] Arash Hajisharifi, Francesco Romanò, Michele Girfoglio, Andrea Beccari, Domenico Bonanni, and Gianluigi Rozza. A non-intrusive data-driven reduced order model for parametrized cfd-dem numerical simulations. *Journal of Computational Physics*, 491:112355, 2023.

[39] Arash Hajisharifi, Rahul Halder, Michele Girfoglio, Andrea Beccari, Domenico Bonanni, and Gianluigi Rozza. An lstm-enhanced surrogate model to simulate the dynamics of particle-laden fluid systems. *Computers & Fluids*, 280:106361, 2024.

[40] Nicola Demo, Marco Tezzele, Gianluca Gustin, Gianpiero Lavini, and Gianluigi Rozza. Shape optimization by means of proper orthogonal decomposition and dynamic mode decomposition. *Technology and Science for the Ships of the Future: Proceedings of NAV 2018: 19th International Conference on Ship & Maritime Research*, page 212–219, 2018.

[41] Matteo Ripepi, Mark Johannes Verveld, NW Karcher, Thomas Franz, Mohammad Abu-Zurayk, Stefan Görtz, and TM Kier. Reduced-order models for aerodynamic applications, loads and mdo. *CEAS Aeronautical Journal*, 9(1):171–193, 2018.

[42] Kookjin Lee and Kevin T Carlberg. Model reduction of dynamical systems on nonlinear manifolds using deep convolutional autoencoders. *Journal of Computational Physics*, 404:108973, 2020.

[43] Stefania Fresca, Luca Dede', and Andrea Manzoni. A comprehensive deep learning-based approach to reduced order modeling of nonlinear time-dependent parametrized PDEs. *Journal of Scientific Computing*, 87(2):1–36, 2021.

[44] Rakesh Halder, Krzysztof J Fidkowski, and Kevin J Maki. Non-intrusive reduced-order modeling using convolutional autoencoders. *International Journal for Numerical Methods in Engineering*, 123(21):5369–5390, 2022.

[45] Romit Maulik, Bethany Lusch, and Prasanna Balaprakash. Reduced-order modeling of advection-dominated systems with recurrent neural networks and convolutional autoencoders. *Physics of Fluids*, 33(3), 2021.

[46] Geoffrey E Hinton and Ruslan R Salakhutdinov. Reducing the dimensionality of data with neural networks. *science*, 313(5786):504–507, 2006.

[47] Hamidreza Eivazi, Hadi Veisi, Mohammad Hossein Naderi, and Vahid Esfahanian. Deep neural networks for nonlinear model order reduction of unsteady flows. *Physics of Fluids*, 32(10), 2020.

[48] Xiaojiao Mao, Chunhua Shen, and Yu-Bin Yang. Image restoration using very deep convolutional encoder-decoder networks with symmetric skip connections. *Advances in neural information processing systems*, 29, 2016.

[49] Yifei Zhang. A better autoencoder for image: Convolutional autoencoder. In *ICONIP17-DCEC. Available online: http://users. cecs. anu. edu. au/Tom. Gedeon/conf/ABCs2018/paper/ABCs2018_paper_58. pdf (accessed on 23 March 2017)*, 2018.

[50] William D Fries, Xiaolong He, and Youngsoo Choi. Lasdi: Parametric latent space dynamics identification. *Computer Methods in Applied Mechanics and Engineering*, 399:115436, 2022.

[51] Francisco J Gonzalez and Maciej Balajewicz. Deep convolutional recurrent autoencoders for learning low-dimensional feature dynamics of fluid systems. *arXiv preprint arXiv:1808.01346*, 2018.

[52] Noriyasu Omata and Susumu Shirayama. A novel method of low-dimensional representation for temporal behavior of flow fields using deep autoencoder. *Aip Advances*, 9(1), 2019.

[53] Herbert Jaeger and Harald Haas. Harnessing nonlinearity: Predicting chaotic systems and saving energy in wireless communication. *science*, 304(5667):78–80, 2004.

[54] Benjamin Schrauwen, David Verstraeten, and Jan Van Campenhout. An overview of reservoir computing: theory, applications and implementations. In *Proceedings of the 15th european symposium on artificial neural networks. p. 471-482 2007*, pages 471–482, 2007.

[55] Mantas Luko*v*sevi*v*cius and Herbert Jaeger. Reservoir computing approaches to recurrent neural network training. *Computer science review*, 3(3):127–149, 2009.

[56] Gouhei Tanaka, Toshiyuki Yamane, Jean Benoit Héroux, Ryosho Nakane, Naoki Kanazawa, Seiji Takeda, Hidetoshi Numata, Daiju Nakano, and Akira Hirose. Recent advances in physical reservoir computing: A review. *Neural Networks*, 115:100–123, 2019.

[57] Sepp Hochreiter and Jürgen Schmidhuber. Long short-term memory. *Neural computation*, 9(8):1735–1780, 1997.

[58] Suraj Pawar, Shady E Ahmed, Omer San, and Adil Rasheed. Data-driven recovery of hidden physics in reduced order modeling of fluid flows. *Physics of Fluids*, 32(3), 2020.

[59] Kai Li, Jiaqing Kou, and Weiwei Zhang. Deep neural network for unsteady aerodynamic and aeroelastic modeling across multiple mach numbers. *Nonlinear Dynamics*, 96:2157–2177, 2019.

[60] Kyunghyun Cho, Bart Van Merriënboer, Caglar Gulcehre, Dzmitry Bahdanau, Fethi Bougares, Holger Schwenk, and Yoshua Bengio. Learning phrase representations using rnn encoder-decoder for statistical machine translation. *arXiv preprint arXiv:1406.1078*, 2014.

[61] Ashish Vaswani, Noam Shazeer, Niki Parmar, Jakob Uszkoreit, Llion Jones, Aidan N Gomez, Łukasz Kaiser, and Illia Polosukhin. Attention is all you need. *Advances in neural information processing systems*, 30, 2017.

[62] Nicholas Geneva and Nicholas Zabaras. Transformers for modeling physical systems. *Neural Networks*, 146:272–289, 2022.

[63] R Hassanian, H Myneni, A Helgadóttir, and M Riedel. Deciphering the dynamics of distorted turbulent flows: Lagrangian particle tracking and chaos prediction through transformer-based deep learning models. *Physics of Fluids*, 35(7), 2023.

[64] Rakesh Sarma, Fabian Hübenthal, Eray Inanc, and Andreas Lintermann. Prediction of turbulent boundary layer flow dynamics with transformers. *Mathematics*, 12(19):2998, 2024.

[65] Mustafa Z Yousif, Meng Zhang, Linqi Yu, Ricardo Vinuesa, and HeeChang Lim. A transformer-based synthetic-inflow generator for spatially developing turbulent boundary layers. *Journal of Fluid Mechanics*, 957:A6, 2023.

[66] Moaad Khamlich, Federico Pichi, Michele Girfoglio, Annalisa Quaini, and Gianluigi Rozza. Optimal transport-based displacement interpolation with data augmentation for reduced order modeling of nonlinear dynamical systems. *arXiv preprint arXiv:2411.08750*, 2024.

[67] Nicola Clinco, Michele Girfoglio, Annalisa Quaini, and Gianluigi Rozza. Filter stabilization for the mildly compressible euler equations with application to atmosphere dynamics simulations. *Computers & Fluids*, 266:106057, 2023.

[68] Michele Girfoglio, Annalisa Quaini, and Gianluigi Rozza. Validation of an OpenFOAM®-based solver for the Euler equations with benchmarks for mesoscale atmospheric modeling. *AIP Advances*, 13(5), 2023.

[69] Simone Marras, Murtazo Nazarov, and Francis X Giraldo. Stabilized high-order Galerkin methods based on a parameter-free dynamic SGS model for LES. *Journal of Computational Physics*, 301:77–101, 2015.

[70] Suhas V Patankar and D Brian Spalding. A calculation procedure for heat, mass and momentum transfer in three-dimensional parabolic flows. In *Numerical prediction of flow, heat transfer, turbulence and combustion*, pages 54–73. Elsevier, 1983.

[71] Raad I Issa. Solution of the implicitly discretised fluid flow equations by operator-splitting. *Journal of computational physics*, 62(1):40–65, 1986.

[72] Fadl Moukalled, Luca Mangani, Marwan Darwish, F Moukalled, L Mangani, and M Darwish. *The finite volume method*. Springer, 2016.

[73] Michele Girfoglio, Annalisa Quaini, and Gianluigi Rozza. A comparative computational study of different formulations of the compressible euler equations for mesoscale atmospheric flows in a finite volume framework. *Computers & Fluids*, 288:106510, 2025.

[74] GEA - Geophysical and Environmental Applications. https://github.com/GEA-Geophysical-and-Environmental-Apps/GEA.

[75] Michele Girfoglio, Annalisa Quaini, and Gianluigi Rozza. GEA: a new finite volume-based open source code for the numerical simulation of atmospheric and ocean flows. In *Finite Volumes for Complex Applications X – Volume 2, Hyperbolic and Related Problems*, pages 151–159. Springer, 2023.

[76] Bethany Lusch, J Nathan Kutz, and Steven L Brunton. Deep learning for universal linear embeddings of nonlinear dynamics. *Nature communications*, 9(1):4950, 2018.

[77] Karen Simonyan and Andrew Zisserman. Very deep convolutional networks for large-scale image recognition. *arXiv preprint arXiv:1409.1556*, 2014.

[78] M Swapna, Yogesh Kumar Sharma, and BMG Prasadh. Cnn architectures: Alex net, le net, vgg, google net, res net. *Int. J. Recent Technol. Eng*, 8(6):953–960, 2020.

[79] Kaiming He, Xiangyu Zhang, Shaoqing Ren, and Jian Sun. Deep residual learning for image recognition. In *Proceedings of the IEEE conference on computer vision and pattern recognition*, pages 770–778, 2016.

[80] Gao Huang, Zhuang Liu, Laurens Van Der Maaten, and Kilian Q Weinberger. Densely connected convolutional networks. In *Proceedings of the IEEE conference on computer vision and pattern recognition*, pages 4700–4708, 2017.

[81] Herbert Jaeger. *Tutorial on training recurrent neural networks, covering BPPT, RTRL, EKF and the echo state network approach*, volume 5. Citeseer, 2002.

[82] David Verstraeten, Benjamin Schrauwen, Michiel d'Haene, and Dirk Stroobandt. An experimental unification of reservoir computing methods. *Neural networks*, 20(3):391–403, 2007.

[83] Herbert Jaeger. The "echo state" approach to analysing and training recurrent neural networks-with an erratum note. *Bonn, Germany: German National Research Center for Information Technology GMD Technical Report*, 148(34):13, 2001.

[84] Nathan Trouvain, Nicolas Rougier, and Xavier Hinaut. Create efficient and complex reservoir computing architectures with reservoirpy. In *International Conference on Simulation of Adaptive Behavior*, pages 91–102. Springer, 2022.

[85] Nashat N Ahmad and John Lindeman. Euler solutions using flux-based wave decomposition. *International Journal for Numerical Methods in Fluids*, 54(1):47–72, 2007.

[86] Nashat N Ahmad. High-resolution wave propagation method for stratified flows. In *2018 Atmospheric and Space Environments Conference*, page 3498, 2018.

[87] Yongliang Feng, Johann Miranda-Fuentes, Jérôme Jacob, and Pierre Sagaut. Hybrid lattice Boltzmann model for atmospheric flows under anelastic approximation. *Physics of Fluids*, 33(3):036607, 2021.

[88] Richard L Carpenter Jr, Kelvin K Droegemeier, Paul R Woodward, and Carl E Hane. Application of the piecewise parabolic method (PPM) to meteorological modeling. *Monthly Weather Review*, 118(3):586–612, 1990.

[89] Francis X Giraldo and Marco Restelli. A study of spectral element and discontinuous Galerkin methods for the Navier–Stokes equations in nonhydrostatic mesoscale atmospheric modeling: Equation sets and test cases. *Journal of Computational Physics*, 227(8):3849–3877, 2008.

[90] Simone Marras, Margarida Moragues, Mariano Vázquez, Oriol Jorba, and Guillaume Houzeaux. A variational multiscale stabilized finite element method for the solution of the euler equations of nonhydrostatic stratified flows. *Journal of Computational Physics*, 236:380–407, 2013.

[91] Jerry M Straka, Robert B Wilhelmson, Louis J Wicker, John R Anderson, and Kelvin K Droegemeier. Numerical solutions of a non-linear density current: A benchmark solution and comparisons. *International Journal for Numerical Methods in Fluids*, 17(1):1–22, 1993.

[92] Lu Lu, Pengzhan Jin, Guofei Pang, Zhongqiang Zhang, and George Em Karniadakis. Learning nonlinear operators via deeponet based on the universal approximation theorem of operators. *Nature machine intelligence*, 3(3):218–229, 2021.

[93] Somdatta Goswami, Katiana Kontolati, Michael D Shields, and George Em Karniadakis. Deep transfer operator learning for partial differential equations under conditional shift. *Nature Machine Intelligence*, 4(12):1155–1164, 2022.

[94] Zongyi Li, Nikola Kovachki, Kamyar Azizzadenesheli, Burigede Liu, Kaushik Bhattacharya, Andrew Stuart, and Anima Anandkumar. Fourier neural operator for parametric partial differential equations, arxiv. *arXiv preprint arXiv:2010.08895*, 2020.